

Ditantalum Hydride Complexes with Bridging (2,6-ⁱPr₂C₆H₃)NSiHPh Silanimine Ligands Resulting from PhSiH₃–Imido Ligand Coupling. A Combined Spectroscopic and Theoretical Investigation

Urs Burckhardt, Gary L. Casty, and T. Don Tilley*

Department of Chemistry, University of California at Berkeley,
Berkeley, California 94720-1460

Tom K. Woo and Ursula Rothlisberger*

Laboratory of Inorganic Chemistry, ETH Zentrum, Universitätsstrasse 6,
8092 Zürich, Switzerland

Received May 30, 2000

The preparation and characterization of two novel dinuclear tantalum hydride complexes featuring bridging silanimine ligands are reported. The reaction of Cp*(ArN=)Ta[Si(SiMe₃)₃]H (Cp* = η⁵-C₅Me₅; Ar = 2,6-ⁱPr₂C₆H₃) with PhSiH₃ resulted in formation of [Cp*(ArN=)TaH(μ-H)]₂ (4% yield), yellow, paramagnetic Cp*₂(ArN=)Ta₂H₂(μ-ArNSiHPh) (**1**, 18% yield), and dark green, diamagnetic Cp*₂Ta₂H₂(μ-ArNSiHPh)₂ (**2**, 71% yield). For **1** and **2**, X-ray structure determinations characterize the ArNSiHPh silanimine ligand as possessing a Si–N single bond. This is confirmed by molecular orbital calculations that provide an average bond order of 0.7 for the Si–N bond. The ArNSiHPh fragment is therefore best viewed as a bifunctional silyl–amido ligand. For diamagnetic complex **2**, the X-ray analysis revealed a molecular structure possessing nearly exact 2-fold symmetry (the hydride ligands were not located), while NMR spectroscopy indicates that the two Cp*Ta(μ-ArNSiHPh) fragments in the molecule are chemically inequivalent. To analyze the structure and bonding in this compound, a theoretical study based on density functional theory and ab initio molecular dynamics was carried out. Calculations of the entire 140-atom dinuclear tantalum system confirm a structure with an asymmetric substitution of the two hydride ligands, with one terminal and one bridging. The paramagnetic compound **1** exhibits structural features that are similar to those for **2**. For this complex, the spectroscopic data and density functional calculations are consistent with a structure featuring terminal and bridging hydride ligands.

Molecular d⁰ metal chemistry has expanded rapidly in recent years, as it has become increasingly apparent that d⁰ centers can mediate a number of bond-forming transformations despite being inactive in oxidative addition–reductive elimination cycles. This chemistry has allowed the development of various catalytic reactions (e.g., olefin polymerization,¹ carbon–carbon coupling,² olefin metatheses,³ hydrogenations,^{2,4} hydrosilations,⁵ and dehydropolymerizations⁶) which feature migratory insertions, cycloadditions, and/or σ-bond metathesis. Despite the considerable attention that early transition metal chemistry has received, surprisingly

little is known about the influence of ancillary ligands on reactivity. We have been particularly interested in delineating electronic and steric factors that control the course of σ-bond metathesis reactions involving d⁰ metal centers. In this context, we have recently begun to explore the chemistry of M–Si and M–H bonds in complexes supported by ancillary imido ligands.^{7–9}

Early transition metal imido complexes have attracted considerable recent attention,¹⁰ and such complexes have led to the development of efficient alkene metathesis catalysts.³ However, d⁰ imido complexes

(1) (a) Brintzinger, H. H.; Fischer, D.; Mulhaupt, R.; Rieger, B.; Waymouth, R. *Angew. Chem., Int. Ed. Engl.* **1995**, *34*, 1143. (b) Jordan, R. F. *Adv. Organomet. Chem.* **1991**, *32*, 325. (c) Kaminsky, W. *Catal. Today* **1994**, *20*, 257. (d) Piers, W. E. *Chem. Eur. J.* **1998**, *4*, 13.

(2) Hoveyda, A. H.; Morken, J. P. *Angew. Chem., Int. Ed. Engl.* **1996**, *35*, 1262.

(3) (a) Ivin, K. J. *Olefin Metathesis and Metathesis Polymerization*; Academic Press: San Diego, 1997. (b) Grubbs, R. H.; Tumas, W. *Science* **1989**, *243*, 907. (c) Schrock, R. R. *Acc. Chem. Res.* **1990**, *23*, 158. (d) Schrock, R. R. *Tetrahedron* **1999**, *55*, 8141. (e) Schuster, M.; Blechert, S. *Angew. Chem., Int. Ed. Engl.* **1997**, *36*, 2036.

(4) (a) Lin, Z.; Marks, T. J. *J. Am. Chem. Soc.* **1987**, *109*, 7979. (b) Lee, N. E.; Buchwald, S. L. *J. Am. Chem. Soc.* **1994**, *116*, 5985.

(5) (a) Fu, P.-F.; Brard, L.; Li, Y.; Marks, T. J. *J. Am. Chem. Soc.* **1995**, *117*, 7157. (b) Molander, G. A.; Julius, M. *J. Org. Chem.* **1992**, *57*, 6347. (c) Molander, G. A.; Dowdy, E. D.; Noll, B. C. *Organometallics* **1998**, *17*, 3754. (d) Carter, M. B.; Schiott, B.; Gutierrez, A.; Buchwald, S. L. *J. Am. Chem. Soc.* **1994**, *116*, 11667.

(6) (a) Gauvin, F.; Harrod, J. F.; Woo, H. G. *Adv. Organomet. Chem.* **1998**, *42*, 363. (b) Tilley, T. D. *Acc. Chem. Res.* **1993**, *26*, 22. (c) Corey, J. In *Advances in Silicon Chemistry*; Larson, G., Ed.; JAI Press: Greenwich, CT, 1991; Vol. 1, p 327.

(7) Casty, G. L.; Tilley, T. D.; Yap, G. P. A.; Rheingold, A. L. *Organometallics* **1997**, *16*, 4746.

(8) Burckhardt, U.; Tilley, T. D. *J. Am. Chem. Soc.* **1999**, *121*, 6328.

(9) Burckhardt, U.; Casty, G. L.; Tilley, T. D. Manuscript in preparation.

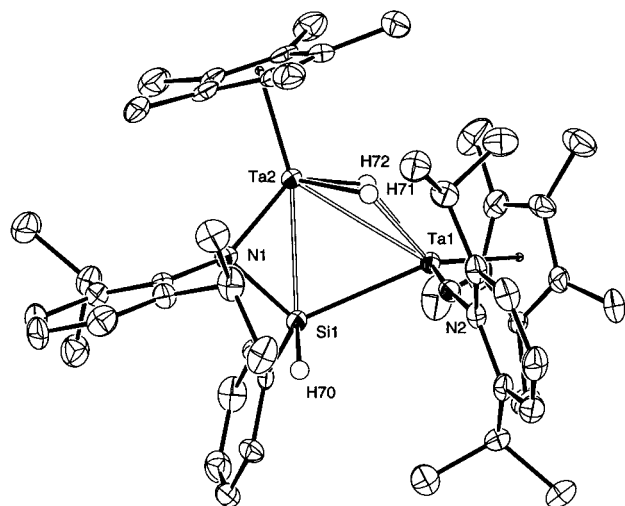


Figure 1. ORTEP diagram of $\text{Cp}^*(\text{ArN}=\text{Ta})_2\text{H}_2(\mu\text{-ArN-SiHPh})$ (**1**).

tion of products (by NMR spectroscopy of the reaction mixture). Thus, the same product ratio was obtained with substoichiometric quantities of PhSiH_3 and when the reaction was carried out in neat PhSiH_3 . However, the product distribution does depend on the reaction time. While $[\text{Cp}^*(\text{ArN}=\text{Ta})\text{H}(\mu\text{-H})]_2$ is generated immediately upon addition of the silane, the hydrides **1** and **2** form more slowly and in an approximately constant ratio, as shown by NMR analysis of the cooled reaction solution at various time intervals.

At this point, the detailed mechanism of the reaction in Scheme 1 is unknown. As expected, the reaction produces a quantitative amount of $\text{HSi}(\text{SiMe}_3)_3$ and elemental hydrogen (by NMR spectroscopy and GC/MS), but oligosilanes (which might be expected to form via silane dehydrocoupling⁶) were not observed. Reaction of the deuteride $\text{Cp}^*(\text{ArN}=\text{Ta})[\text{Si}(\text{SiMe}_3)_3]\text{D}$ with PhSiH_3 produced mainly $\text{DSi}(\text{SiMe}_3)_3$ (80%), but minor quantities of $\text{PhSiH}_{3-n}\text{D}_n$ ($n = 1-3$) and HD were also observed (by ^1H and ^2H NMR spectroscopy). Upon reaction of $\text{Cp}^*(\text{ArN}=\text{Ta})[\text{Si}(\text{SiMe}_3)_3]\text{D}$ with PhSiD_3 , no $\text{HSi}(\text{SiMe}_3)_3$ was observed as product. This finding suggests the operation of competing pathways (including reductive elimination–oxidative addition and/or σ -bond metathesis) and is similar to observations made in the reaction of the 16-electron hafnocene $\text{CpCp}^*\text{Hf}[\text{Si}(\text{SiMe}_3)_3]\text{H}$ with $\text{H}_2\text{Si}(\text{SiMe}_3)_2$.¹³ Attempts to convert $[\text{Cp}^*(\text{ArN}=\text{Ta})\text{H}(\mu\text{-H})]_2$ and **1** to the main product **2** by heating them in the presence of PhSiH_3 failed; there was no conversion even after refluxing in benzene for several days. The addition of hydrogen, $\text{HSi}(\text{SiMe}_3)_3$, or small amounts of AIBN did not initiate the reaction.

Characterization of 1. The molecular structure of **1** was determined by X-ray crystallography (Figure 1). Important bond distances and angles are listed in Table 1. The two tantalum atoms are separated by a distance of 3.0190(3) Å and are bridged by the unusual μ, η^2 - ArNSiHPh silanimine ligand. Bonding of the latter bridging ligand to the two tantalum centers results in a “five-coordinate” silicon and similar Ta–Si bond lengths (Si–Ta(1) = 2.709(1) Å; Si–Ta(2) = 2.648(1) Å). These Ta–Si distances correspond to normal, single

Table 1. Selected Bond Lengths (Å) and Angles (deg) for Compound **1**^a

Bond Length			
Ta(1)–Ta(2)	3.0190(3)	N(1)–C(27)	1.423(6)
Ta(1)–Si(1)	2.709(1)	N(2)–C(39)	1.401(6)
Ta(1)–N(2)	1.812(4)	Ta(1)–H(71)	1.95(5)
Ta(1)–Cp*(1) _{cent}	2.1605(2)	Ta(1)–H(72)	2.17(5)
Ta(2)–Si(1)	2.648(1)	Ta(2)–H(71)	1.79(5)
Ta(2)–N(1)	1.963(4)	Ta(2)–H(72)	1.72(5)
Ta(2)–Cp*(2) _{cent}	2.1088(2)	Si(1)–H(70)	1.42(5)
Si(1)–N(1)	1.832(4)		
Bond Angles			
Ta(2)–Ta(1)–Si(1)	54.75(3)	Si(1)–Ta(1)–H(71)	75(1)
Ta(2)–Ta(1)–N(2)	110.2(1)	Si(1)–Ta(1)–H(72)	76(1)
Ta(2)–Ta(1)–Cp*(1) _{cent}	126.95(1)	N(2)–Ta(1)–H(71)	82(1)
Si(1)–Ta(1)–N(2)	95.1(1)	N(2)–Ta(1)–H(72)	140(1)
Si(1)–Ta(1)–Cp*(1) _{cent}	134.15(3)	Cp*(2) _{cent} –Ta(2)–H(71)	108(1)
N(2)–Ta(1)–Cp*(1) _{cent}	118.5(1)	Cp*(2) _{cent} –Ta(2)–H(72)	111(2)
Ta(1)–Ta(2)–Si(1)	56.65(3)	H(71)–Ta(2)–H(72)	71(2)
Ta(1)–Ta(2)–N(1)	97.9(1)	Ta(1)–Si(1)–H(70)	102(2)
Ta(1)–Ta(2)–Cp*(2) _{cent}	137.10(1)	Ta(2)–Si(1)–H(70)	131(2)
Si(1)–Ta(2)–N(1)	43.8(1)	N(1)–Si(1)–H(70)	104(2)
Si(1)–Ta(2)–Cp*(2) _{cent}	163.50(3)	Cp*(1) _{cent} –Ta(1)–H(71)	136(1)
N(1)–Ta(2)–Cp*(2) _{cent}	119.9(1)	Cp*(1) _{cent} –Ta(1)–H(72)	93(1)
Ta(1)–Si(1)–Ta(2)	68.60(3)	H(71)–Ta(1)–H(72)	59(2)
Ta(1)–Si(1)–N(1)	113.1(1)	N(1)–Ta(2)–H(71)	38(1)
Ta(2)–Si(1)–N(1)	47.8(1)	Ta(1)–Ta(2)–H(72)	45(2)
Ta(2)–N(1)–Si(1)	88.4(2)	Si(1)–Ta(2)–H(71)	79(1)
Ta(2)–N(1)–C(27)	150.4(3)	Si(1)–Ta(2)–H(72)	85(2)
Ta(1)–N(2)–C(39)	170.4(3)	N(1)–Ta(2)–H(71)	104(1)
Ta(2)–Ta(1)–H(71)	34(1)	N(1)–Ta(2)–H(72)	127(2)
Ta(2)–Ta(1)–H(72)	34(1)		

^a $\text{Cp}^*_{\text{cent}}$ represents the average of the x , y , and z coordinates of the $\eta^5\text{-C}_5\text{Me}_5$ ring carbons.

covalent bonds, as seen by comparisons to structurally characterized tantalum silyls such as $\text{Cp}^*\text{Cl}_3\text{TaSiMe}_3$ (Ta–Si = 2.669(4) Å).¹⁴ This bridging interaction results in a very acute Ta(1)–Si(1)–Ta(2) bond angle of 68.60(3)°. The silanimine ligand appears to possess very little Si=N double bond character, as indicated by the Si(1)–N(1) bond length of 1.832(4) Å. For comparison, the Si=N bond length in $^t\text{Bu}_2\text{Si}=\text{NSi}^t\text{Bu}_3$ is only 1.568(3) Å,¹⁵ and the corresponding distance in the mononuclear silanimine complex $\text{Cp}_2\text{Zr}(\eta^2\text{-Me}_2\text{Si}=\text{N}^t\text{Bu})(\text{CO})$ is 1.661(4) Å.¹⁶ In addition, the Ta(2)–N(1) bond length of 1.963(4) Å is consistent with a Ta(IV)–N single covalent bond, as seen (for example) by comparisons to the Ta–N distances of 1.97–1.99 Å in the related ditantalum hydride $[(\text{Cy}_2\text{N})_2\text{CITa}(\mu\text{-H})]_2$.^{12g} Thus, the silanimine ligand in **1** is best viewed as a bridging silyl–amido ligand, with single covalent Ta–Si, Ta–N, and Si–N bonds. The arylimido ligand in **1** is bound to Ta(1) in the usual way, as indicated by the nearly linear Ta(1)–N(2)–C(39) angle (170.4(3)°) and the short Ta(1)–N(2) distance of 1.812(4) Å. For comparison, the Ta(2)–N(1)–C(27) angle is 150.4(3)° and the Ta(2)–N(1) distance is 1.963(4) Å. The difference electron density map contained two peaks that were assigned to the hydride ligands. Both hydrides were characterized as asymmetrically bridging the two tantalum atoms such that they are closer to Ta(2): Ta(2)–H(71) = 1.79(5) Å; Ta(1)–H(71) = 1.95(5) Å; Ta(2)–H(72) = 1.72(5) Å; Ta(1)–H(72) = 2.17(5) Å. Note, however, that infrared

(14) Arnold, J.; Shina, D. N.; Tilley, T. D.; Arif, A. M. *Organometallics* **1986**, *5*, 2037.

(15) Wiberg, N.; Schurz, K.; Reber, G.; Müller, G. *J. Chem. Soc., Chem. Commun.* **1986**, 591.

(16) Procopio, L. J.; Carroll, P. J.; Berry, D. H. *Polyhedron* **1995**, *14*, 45.

(13) Casty, G. L.; Lugmair, C. G.; Radu, N. S.; Tilley, T. D.; Walzer, J. F.; Zargarian, D. *Organometallics* **1997**, *16*, 8.

data and density functional calculations suggest that one of the hydride ligands might best be described as terminal (vide infra).

The infrared spectrum exhibits a weak Si–H stretch at 2173 cm^{-1} , and two broad bands at 1763 and 1653 cm^{-1} are assigned to the two hydride ligands. While the higher frequency Ta–H vibration falls well within the range expected for a terminal tantalum hydride, the lower one lies somewhere between those for a terminal and a bridged Ta–H stretch.¹² For comparison, the hydride $[\text{Cp}^*(\text{ArN}=\text{TaH}(\mu\text{-H}))_2]$ exhibits infrared ν_{TaH} stretching bands at 1529 cm^{-1} (bridging) and 1771 cm^{-1} (terminal).⁹

Because of the paramagnetic nature of compound **1**, its NMR spectra feature only broad signals, which sharpen somewhat with increases in temperature. The ^1H NMR spectrum contains two very broad signals at 10.5 and 0.2 ppm, which each integrate to one hydrogen and are attributed to the two hydride ligands. The Si–H resonance appears at 4.93 ppm (singlet) and displays satellites reflecting a $^1J_{\text{SiH}}$ coupling constant of 220 Hz. Resonances for the two Cp* ligands are observed at 2.14 and 1.95 ppm. Low signal intensities due to the paramagnetism of **1** precluded direct measurements of the ^{13}C and ^{29}Si NMR spectra; however, the heteroatoms bound to hydrogen were conveniently observed via H,X HMQC experiments. Thus, the methyl Cp* resonance was observed at 12.6 ppm as a single peak, and the chemical shift for the silicon atom was determined to be 9.7 ppm.

The magnetic moment of **1** was determined to be $\mu_{\text{eff}} = 2.0\ \mu_{\text{B}}$ (per dimer, by the Evans method¹⁷ at $24\text{ }^\circ\text{C}$). This value is quite low and incompatible with two independent Ta(IV) centers, and suggests the presence of a weak antiferromagnetic interaction between the tantalum atoms. This μ_{eff} value does not change with temperature, up to $90\text{ }^\circ\text{C}$.

Theoretical Characterization of 1. Although the positions of the hydrides in paramagnetic complex **1** were determined by the X-ray diffraction analysis, there is uncertainty in these assignments due to the proximity of the hydrides to the heavy Ta atoms. Additionally, the characterization of both hydrides as bridging the tantalum centers is at odds with what is suggested by the infrared data. For these reasons we examined the paramagnetic complex with density functional theory (see Computational Details in the Experimental Section). In these calculations the actual ligand system was included and the calculations were performed within the spin-unrestricted formalism assuming two unpaired electrons. Full geometry optimization initiated from the experimentally derived structure leads to the geometric parameters given in Figure 2. With the exception of the hydride positions the calculated geometry is in excellent agreement with the experimental structure. The asymmetric bridging arrangement of both hydrides, as determined by the X-ray diffraction analysis, is approximately reproduced. However, the asymmetry involving one of the bridging hydrides, H(72), is so severe that it should be considered a terminal hydride. More specifically, the calculated structure has distances of $\text{Ta}(2)\text{--H}(72) = 2.77$ and $\text{Ta}(1)\text{--H}(72) = 2.94\text{ \AA}$, whereas they

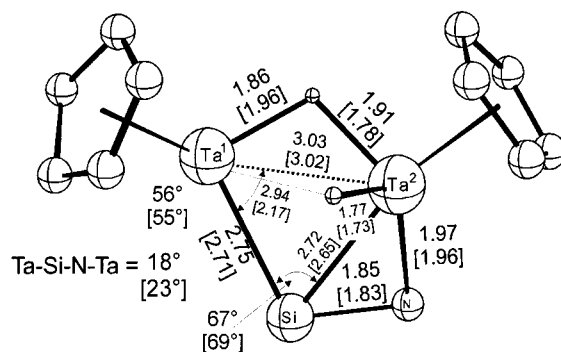


Figure 2. Comparison of the X-ray and theoretical structure of the paramagnetic complex $\text{Cp}^*_2(\text{ArN}=\text{Ta})_2\text{H}_2(\mu\text{-ArNSiHPh})$ (**1**). Pendant groups including the $=\text{NAr}$ moiety have been removed for clarity. The bracketed values are for the experimental X-ray structure.

have been determined to be 2.73 and 2.18 Å from the X-ray analysis. The calculated $\text{Ta}(1)\text{--H}(72)$ distance of 2.94 Å is almost as long as the Ta–Ta distance of 3.02 Å. As previously mentioned, this asymmetry, although in disagreement with the X-ray analysis, is in better agreement with the observed infrared data. We also note that in the calculated structure, the other bridging hydride is found to lie closer to Ta(1), whereas from the X-ray analysis both bridging hydrides were found to lie closer to Ta(2). Besides the hydride positions, other geometric parameters found in the calculated structure are in excellent agreement with the X-ray structure. Most notably, the Ta–Ta distances agree to within 0.01 Å. Additionally, parameters not shown in Figure 2 are also in good agreement, such as the $\text{Ta}(1)\text{--N}(2)\text{--C}(39)$ and $\text{Ta}(2)\text{--N}(1)\text{--C}(27)$ angles, which are calculated to be 170° and 147° and are experimentally determined to be 170° and 150° , respectively.

The nature of the Si–N and Ta–Ta bonds in **1** can be analyzed within the framework of molecular orbital theory. A Mayer bond order analysis¹⁸ provides a qualitative measure of the covalent bond strength between two atoms. As previously stated, the silanimine ligand appears to possess very little Si=N double bond character. This is confirmed by the calculated bond order of 0.75 between Si(1) and N(1). To compare, the calculated bond orders in the same structure are found to be 1.04 for the N(1)–C(aryl) bond, 0.79 for the Si(1)–C(aryl) bond, and 1.36 for the Ta(1)=N(2) double bond. The nature of the Ta–Ta bond is also of interest. The calculated bond order between the Ta–Ta atoms is 0.13, which suggests a very weak covalent bond. Mulliken charges on the two Ta centers are almost identical at +2.9 e, thereby eliminating the possibility of an ionic type of interaction. From this analysis we conclude that there is no significant Ta–Ta bond and that the 3.02 Å interatomic distance is maintained by the bridging Ta–Si interactions.

Since the magnetic moment of **1** ($2.0\ \mu_{\text{B}}$) suggests the presence of weak antiferromagnetic coupling, we have also repeated the above unrestricted calculations starting from the X-ray structure assuming a total spin momentum of zero. This open-shell singlet state calculation also results in a structure that is in good agreement with experiment, again with the exception of the

(17) (a) Evans, D. F. *J. Chem. Soc.* **1959**, 2003. (b) Sur, S. K. *J. Magn. Reson.* **1989**, *82*, 169.

(18) Mayer, I. *Chem. Phys. Lett.* **1983**, *97*, 270–274.

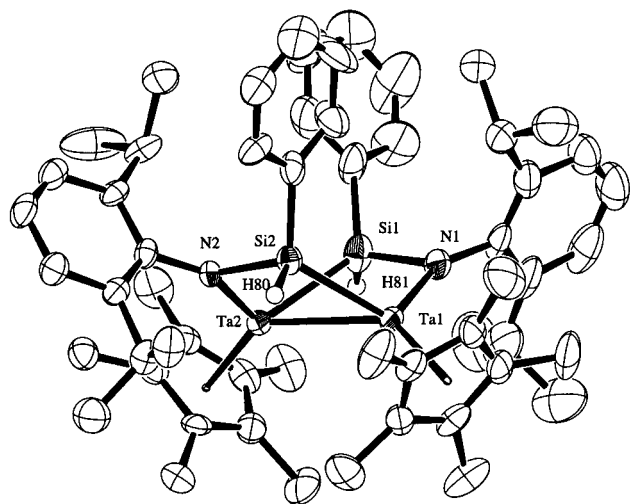


Figure 3. ORTEP diagram of $\text{Cp}^*_2\text{Ta}_2\text{H}_2(\mu\text{-ArNSiHPh})_2$ (**2**).

hydride positions. Similar to the triplet state structure, a complex with one bridging hydride and one hydride that can be considered to be terminal or highly asymmetrically bridging is found. Compared to the triplet state structure, the singlet state structure possesses a slightly longer Ta–Ta bond of 3.14 Å and a longer Ta(1)–H(72) distance of 3.14 Å. (Thus, the hydride in the singlet state structure can be considered more terminal in nature.) Interestingly, the total energy of the singlet complex was only 0.02 kcal/mol higher than that of the triplet complex. The total unpaired spin density, η as given by $\eta = \int |\rho^\alpha(\mathbf{r}) - \rho^\beta(\mathbf{r})| d\mathbf{r}$, was found to be 2.03 e, indicating the presence of an antiferromagnetically coupled state. Considering the very small energy difference between the two states, it is possible that the experiment refers to a mixed state (multi-determinantal), which could give rise to the observed intermediate value of the magnetic moment.

From these calculations, we conclude that the paramagnetic complex possesses a structure in which one hydride is terminal in nature and the other is bridging.

Characterization of 2. The molecular structure of **2** was determined by a single-crystal X-ray diffraction analysis (Figure 3), and selected bond lengths and angles are listed in Table 2. The tantalum atoms are linked by two bridging μ, η^2 -ArNSiHPh ligands, which give the molecule a butterfly conformation such that the two “wings” (defined by the planar Ta_2NSi rings) intersect at a dihedral angle of 67.8°. The interatomic Ta–Ta distance of 2.8472(5) Å is significantly shorter than the corresponding distance in **1** (by 0.17 Å). As can be seen in Figure 3, the molecule possesses approximate (noncrystallographic) 2-fold symmetry. As in **1**, the silicon atoms are pentacoordinate and roughly evenly positioned between the two tantalum atoms (Ta–Si distances range from 2.61 to 2.70 Å). In general, the distances and angles associated with the silanimine ligation are very similar to the corresponding values observed for **1**. Probably due to peripheral noise associated with disordered hexane solvent of crystallization in the structure, the hydride ligands could not be located. Given the observed molecular symmetry, it would seem likely that they adopt symmetrical positions in the complex, either as bridging ligands underneath

Table 2. Selected Bond Lengths (Å) and Angles (deg) for Compound $2 \cdot 2/3\text{C}_6\text{H}_{14}$ ^a

Bond Length			
Ta(1)–Ta(2)	2.8472(5)	Ta(2)–Cp*(2) _{cent}	2.1287(3)
Ta(1)–Si(1)	2.695(3)	Si(1)–N(1)	1.817(8)
Ta(1)–Si(2)	2.614(3)	Si(2)–N(2)	1.824(7)
Ta(1)–N(1)	1.957(7)	N(1)–C(7)	1.43(1)
Ta(1)–Cp*(1) _{cent}	2.1275(3)	N(2)–C(35)	1.45(1)
Ta(2)–Si(1)	2.644(3)	Si(1)–H(81)	1.553
Ta(2)–Si(2)	2.697(2)	Si(2)–H(80)	1.429
Ta(2)–N(2)	1.967(7)		
Bond Angles			
Ta(2)–Ta(1)–Si(1)	56.92(6)	Ta(1)–Ta(2)–Cp*(2) _{cent}	135.39(2)
Ta(2)–Ta(1)–Si(2)	59.00(5)	Si(1)–Ta(2)–Si(2)	88.45(8)
Ta(2)–Ta(1)–N(1)	99.2(2)	Si(1)–Ta(2)–N(2)	115.1(2)
Ta(1)–Si(2)–Ta(2)	64.82(6)	Si(1)–Ta(2)–Cp*(2) _{cent}	113.80(6)
Ta(1)–Si(2)–N(2)	111.6(2)	Si(2)–Ta(2)–N(2)	42.5(2)
Ta(2)–Ta(1)–Cp*(1) _{cent}	135.51(2)	Si(2)–Ta(2)–Cp*(2) _{cent}	157.74(5)
Si(1)–Ta(1)–Si(2)	89.12(8)	N(2)–Ta(2)–Cp*(2) _{cent}	120.6(2)
Si(1)–Ta(1)–N(1)	42.4(2)	Ta(1)–Si(1)–Ta(2)	64.44(6)
Si(1)–Ta(1)–Cp*(1) _{cent}	159.36(6)	Ta(1)–Si(1)–N(1)	46.5(2)
Si(2)–Ta(1)–N(1)	115.3(2)	Ta(2)–Si(1)–N(1)	110.9(3)
Si(2)–Ta(1)–Cp*(1) _{cent}	111.40(5)	Ta(2)–Si(2)–N(2)	46.8(2)
N(1)–Ta(1)–Cp*(1) _{cent}	121.2(2)	Ta(1)–N(1)–Si(1)	91.1(3)
Ta(1)–Ta(2)–Si(1)	58.64(6)	Ta(1)–N(1)–C(7)	150.7(6)
Ta(1)–Ta(2)–Si(2)	56.18(5)	Ta(2)–N(2)–C(35)	148.8(5)
Ta(1)–Ta(2)–N(2)	98.7(2)		

^a Cp*_{cent} represents the average of the *x*, *y*, and *z* coordinates of the $\eta^5\text{-C}_5\text{Me}_5$ ring carbons.

the butterfly wings or terminally bound at each tantalum atom. Surprisingly, however, the spectroscopic data are not consistent with such a symmetric structure.

The ¹H NMR spectrum of **2** contains individual, well-separated sets of resonances for the two halves of the molecule. Most striking is the large separation in shift for the two hydride resonances, which appear at 11.63 ppm (doublet of doublets) and –0.99 ppm (triplet) and exhibit an H–H coupling constant of 2.3 Hz. Resonances for the inequivalent Si–H hydrogens appear at 5.23 (as a doublet of doublets) and 5.09 ppm (as a singlet), with observed satellites that correspond to ¹J_{SiH} coupling constants of 215 and 193 Hz, respectively. Interestingly, only the low-field Si–H group is coupled to the hydride ligands (*J*_{HH} = 5.5 and 2.3 Hz). Two sets of ligand resonances are also observed in the ¹³C and ²⁹Si NMR spectra of **2**, and the latter spectrum exhibits individual resonances at –7.6 and 14.2 ppm, respectively.

The infrared spectrum of **2** contains several weak bands between 1535 and 1792 cm^{–1}, in the regions expected for both terminal and bridging hydride ligands in tantalum complexes, and the Si–H stretching bands for **2** appear at 2145 and 2181 cm^{–1}.

Given the X-ray structural analysis of **2**, the spectroscopically observed asymmetry in the molecule must be generated from the two hydride ligands. However, the data presented above does not allow determination of the hydride ligand positions. A potentially complicating factor in the interpretation of spectroscopic data would be the presence of isomers in the sample. For example, the asymmetric silicon centers in **2** suggest the possible existence of diastereomers. To help address these questions, we recorded the ¹H NMR spectrum of a single crystal of **2**. This spectrum was identical to those of other samples of **2**, indicating that **2** forms as one isomer with a high degree of diastereoselectivity.

With the aid of 2D TOCSY, NOESY, and ¹H, ¹³C HMQC spectra, all proton and carbon resonances for **2**

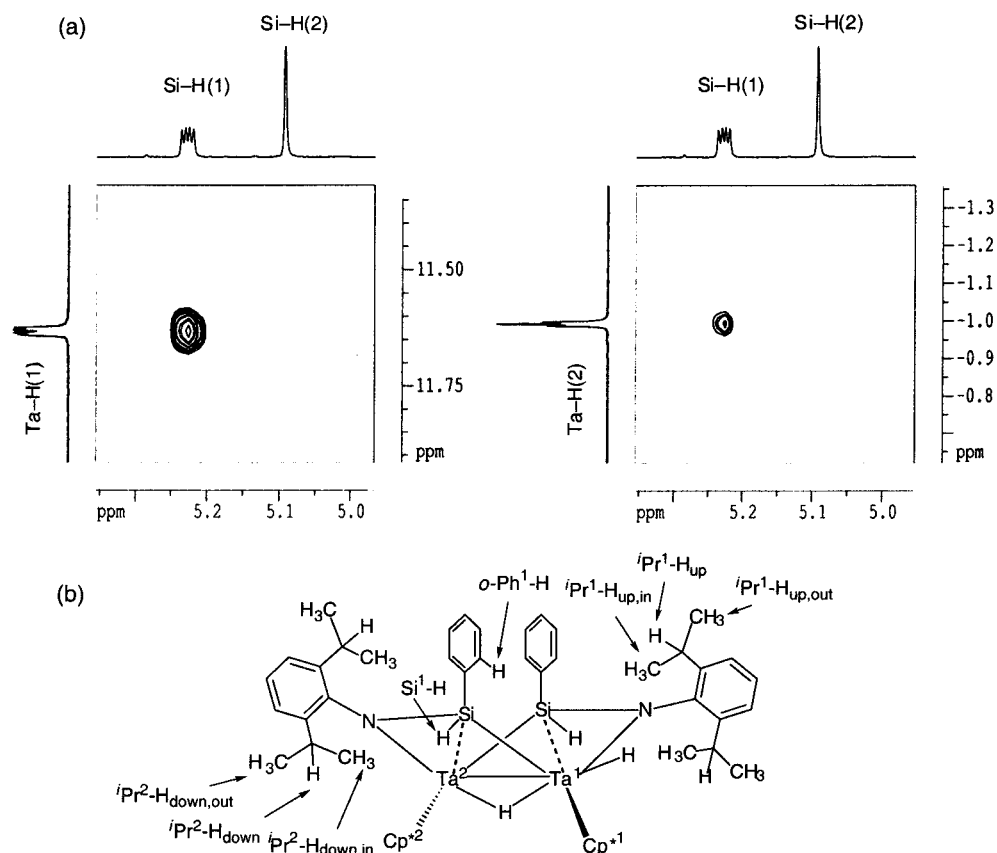


Figure 4. (a) Sections of the 2D NOESY spectra (500 MHz, benzene- d_6 , room temperature, mixing time 0.8 s) of **2**. NOE signals to both hydrides are observed for the lower-field Si-H hydrogen only. (b) Representation of the structure of **2**, illustrating the labeling scheme used to indicate various hydrogens characterized by NOE experiments.

have been assigned. Furthermore, careful evaluation of the NOE signals allowed a determination of the approximate location of the hydride ligands in the molecule. Both hydrides appear to be close to the Si-H hydrogen resonating at 5.23 ppm (to which they also couple), but no NOE signals to the other Si-H resonance were observed (Figure 4). It would appear that the low-field hydride ($\delta = 11.63$ ppm) is in a terminal position and bonded to Ta¹ (Figure 4), oriented away from Ta² and toward the upper ⁱPr¹ group (as evidenced by a strong NOE to Si¹-H and ⁱPr¹-H_{up} and weak NOEs to *o*-Ph¹-H, Cp^{*1}, and ⁱPr¹-Me_{up,out}). The high-field hydride ($\delta = -0.99$ ppm) is located in a region between the two Cp* ligands (weak NOEs to Cp^{*1}, Cp^{*2}, Si¹-H, and ⁱPr²-H_{down}), possibly bridging the Ta atoms (Figure 4). Complex **2** is stereochemically rigid over the temperature range of -60 to 95 °C, as indicated by ¹H NMR spectra (in toluene- d_8).

Thus, the experimental data for **2** are consistent with a structure involving asymmetric substitution of the hydride ligands in the otherwise C_2 -symmetric molecular fragment Cp^{*2}Ta₂(μ -ArNSiHPh)₂. Given this surprising result and the uncertainty in the hydride positions of **2**, the theoretical study presented below was undertaken.

Theoretical Characterization of 2: General Considerations. To determine the most probable position of the tantalum-bound hydrogens in the diamagnetic complex **2**, the geometries of various candidate isomers were optimized at the density functional level, and their relative energies were compared. As a further

scan of the relevant configurational space, we performed elevated temperature ab initio molecular dynamics simulations.¹⁹ With the aim of performing as much as possible an unbiased search, both hydride and dihydrogen complexes have been examined. This includes symmetric structures that are not consistent with the two distinct TaH chemical shifts observed experimentally.

To more efficiently evaluate the relative energies of selected conformers, we have constructed a model system, Cp₂Ta₂H₂(μ -HNSiH₂)₂ (**3**), whereby the aryl and phenyl groups of the full system have been replaced with hydrogen atoms and the Cp* ligands have been replaced with Cp ligands. Using the results from the model system as a guide, we then have examined the actual complex whereby the Cp* and (2,6-ⁱPr₂C₆H₃)NSiHPh ligands are included.

All candidate structures represented in Figure 5 have been examined with the model system. Structures in which the two hydride ligands are positioned approximately endo to the two Cp* rings are shown in Figure 5a, those in which the hydride ligands are both exo to the Cp* rings are displayed in Figure 5b, and candidate structures in which one hydride is positioned endo while the other is positioned exo to the Cp* rings are depicted in Figure 5c. In the following discussion we have adopted an alphanumeric labeling scheme whereby the numeric component refers to either the actual system, **2**, or the model system, **3**, and the alphabetic component refers to the conformation of the hydride ligands as displayed in Figure 5.

(19) Parrinello, M. *Solid State Commun.* **1997**, *102*, 107-120.

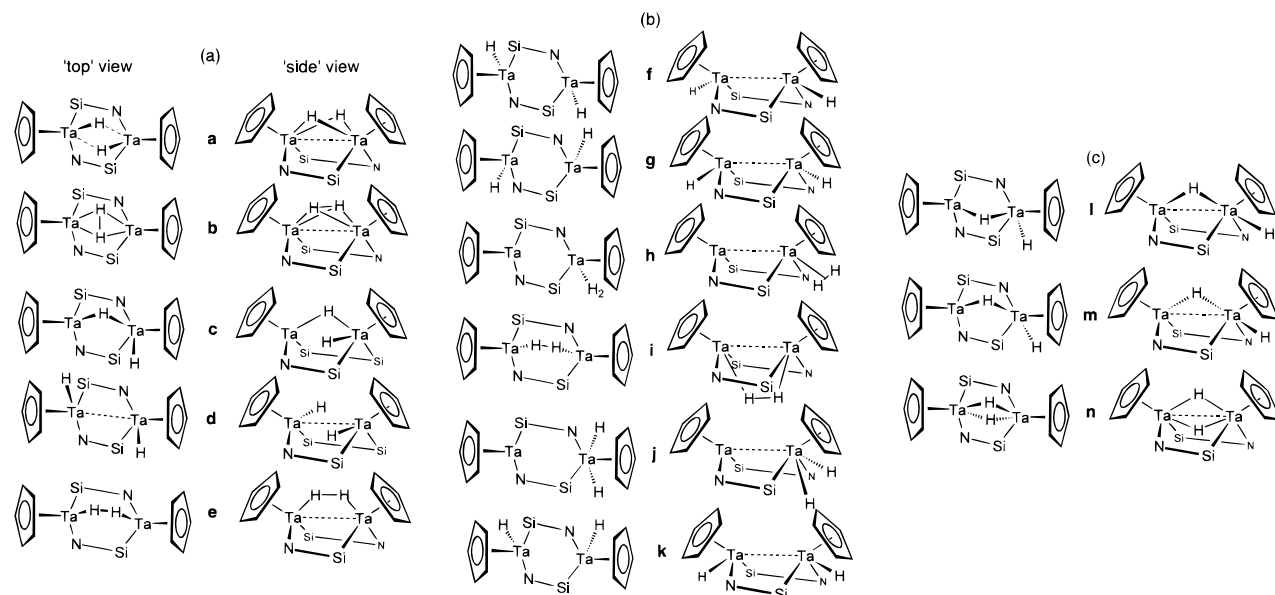


Figure 5. Sketches of candidate isomers of the diamagnetic complex **2** that have been examined by density function theory calculations. (a) Isomers in which both hydrogen atoms are positioned endo to the Cp rings. (b) Isomers that have been investigated in which both hydrogen atoms are positioned exo to the Cp rings. (c) Isomers considered in which one hydrogen atom is positioned exo to the two Cp rings. For each isomer, two orientations are shown and pendant groups have been removed for clarity.

Table 3. Relative DFT-BLYP Energies for Candidate Complexes in the Model (3) and Full (2) Systems

structure ^a	relative energies ^b (kcal/mol)		is optimized structure consistent with NMR data?
	model system (3)	full system (2)	
a	0.0	0.0	no
b–e	converges to 3a	not investigated	N/A
f	+7.9	+3.2	no
g	converges to 3f	not investigated	N/A
h	+45	not investigated	possible ^c
i	H ₂ ejected	not investigated	N/A
j	+5.8	+15	yes ^d
k	converges to 3f	not investigated	N/A
l	+7.3	−0.7	yes
m	converges to 3l	converges to 2l	N/A
n	+34.7	not investigated	yes

^a See Figure 5. ^b DFT BLYP energies relative to isomer **a**. ^c The hydrogens in this dihydrogen complex are inequivalent, but rapid rotation is likely to make them equivalent on the NMR time scale.

^d Inequivalent terminal hydrides are on the same Ta center.

Calculations on the Model System. With the model system, optimization of all structures shown in Figure 5a lead to generation of the bis- μ -dihydride compound **3a**. As it turns out, **3a** is the lowest energy structure that we have located on the potential energy surface of the truncated model system. Thus, in Table 3 we report the energies of all other optimized structures relative to it. We note that the two Ta-bound hydrogens in **3a** are homotopic, and therefore only one NMR chemical shift would be observed for this isomer. In Table 3 we also indicate whether the optimized structure is consistent with the experimental observation of two distinct Ta–H NMR shifts.

Characteristic geometrical parameters of the optimized structure **3a**, compared with that of the X-ray structure **2**, are displayed in Figure 6a. The geometry of the Ta-silanimine six-membered-ring system is reasonably reproduced. The most notable geometric distortions involve the puckering of the ring and the

position of the cyclopentadienyl rings. Compared to the X-ray structure, the Ta-silanimine ring system is more puckered in the optimized geometry of the model structure. This is evidenced by the contracted Ta–Ta bond distance, the diminished N–Ta–Si angles, and the enlarged centroid–Ta–Ta angles. The most severe distortion is the N–Ta–Si angle, which is calculated to be 96° in the model system but is 115° in the experimentally determined structure.

Of the isomers with hydride ligands exo to the cyclopentadienyl rings (Figure 5b), only isomers **3f** and **3j**, which lie 7.9 and 5.8 kcal/mol above **3a**, respectively, are regarded as energetically significant. Geometry optimization of isomer **3f** resulted in two terminal hydrides, which are homotopic. In isomer **3j**, the two terminal hydrides are bound to the same Ta center and are not equivalent. Thus, if no rapid exchange occurs between the hydrides, two distinct Ta–H NMR shifts would be observed. Shown in Figure 6b are selected geometric parameters for the optimized structure of the model system, **3j**. Despite the asymmetric hydride binding in **3j**, the Ta₂N₂Si₂ six-membered ring also remains nearly symmetric. Also notable is that the ring puckering observed in **3j** is less severe than in **3a**.

Of the structures in Figure 5c only **3l**, which lies 7.3 kcal/mol above **3a**, is considered energetically relevant. Structure **3l** is interesting because it contains one terminal hydride and one bridging hydride and is therefore consistent with the observed large difference in Ta–H NMR shifts (11.63 and −0.99 ppm). The optimized structure of **3l** is displayed in Figure 6c. The asymmetric bonding of the two hydrides in **3l** induces a noteworthy asymmetry in the Ta-silanimine ring system, which is highlighted by a 0.1 Å difference in the length of the two Ta–Si bonds.

Ab initio molecular dynamics simulations of the model complexes **3a**, **3f**, and **3l** have been performed at elevated temperatures in order to scan the potential

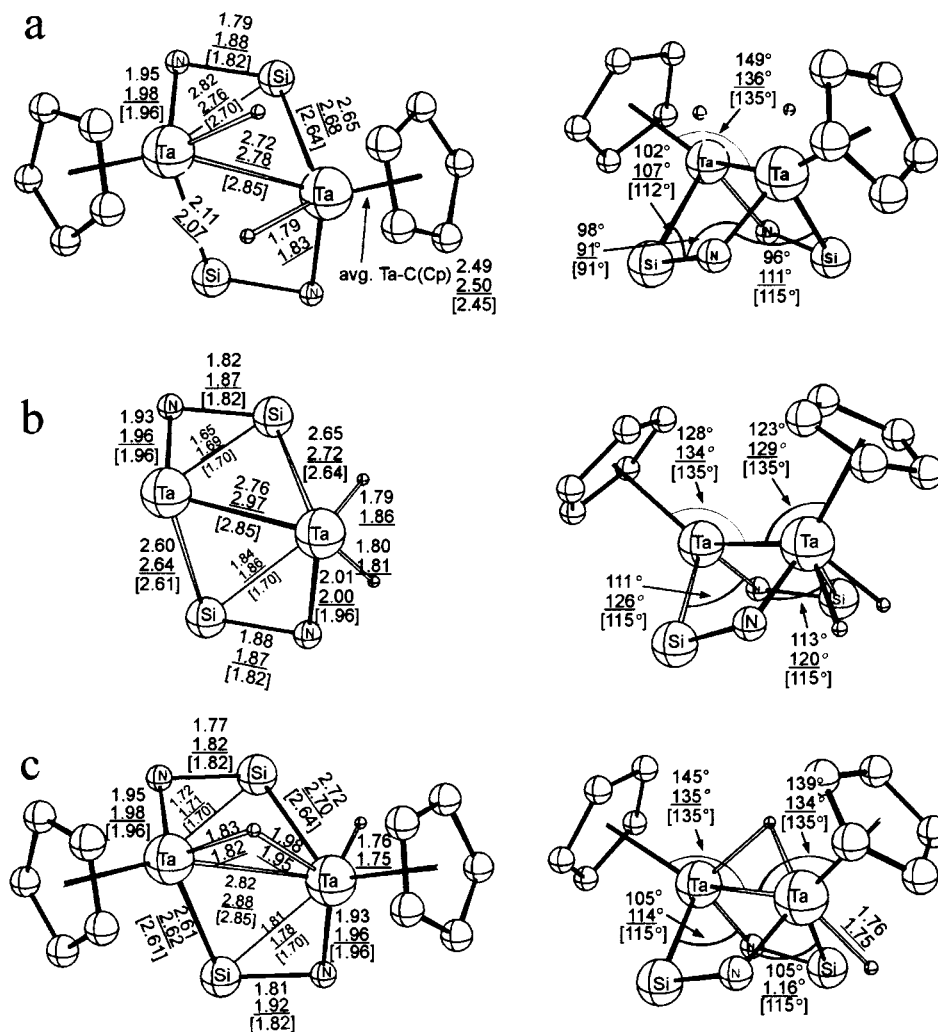


Figure 6. Comparison of selected geometric parameters from the X-ray structure of **2** and the calculated geometries for the model system (**3**) and the actual system (**2**). The comparison is made for isomers **a**, **j**, and **l** in parts a, b, and c, respectively. The right- and left-hand structures are two different views of the same complex. Some pendant groups have been removed for clarity. Plain text values are of the calculated model system, underlined values correspond to the calculated system with the full ligand set, and the bracketed values are of the experimental X-ray structure. For isomer **a** values displayed for the experimental X-ray structure are averages of equivalent parameters, assuming C_2 symmetry.

surface for additional structures that may have been overlooked with the local optimizations. Three 1.5 ps simulations at 600 K initiated from the optimized structures **3a**, **3f**, and **3l**, respectively, revealed no new isomers. Starting from isomer **3a**, an extended simulation totaling 4.0 ps at 900 K also revealed no new isomers. Within these relatively short time scales, the molecular dynamics simulations suggest that the structures are stable and represent well-defined complexes even at elevated temperatures.

Calculations Involving the Actual Ligand System. We have examined the potential surface of the full diamagnetic system (**2**), with no approximations being made for the pendant ligands. The four lowest energy conformers of the model system, **a**, **f**, **j**, and **l** (see Figure 5), were fully optimized, and a summary of the relative energies of the isomers is displayed in the third column of Table 3. The resulting geometric parameters of **2a**, **2j**, and **2l** are also depicted in Figures 6a, 6b and 6c, respectively, and compared with the model system and the X-ray structure.

With the authentic ligand set, the symmetric bis- μ -hydride isomer, **a**, is no longer the most stable complex.

Instead, the asymmetric isomer **2l** is slightly lower in energy on the BLYP-DFT potential energy surface. Also noteworthy is that isomer **j**, which was found to be the second most stable isomer with the model ligand system, lies 15 kcal/mol above isomer **a** with the actual ligand system. Compared to the model system, the geometries obtained with the real ligands tend to be in much better agreement with the X-ray structure. Most significantly, the severe puckering of the $Ta_2N_2Si_2$ rings in model isomers **a** and **l** (as evidenced by the contracted N-Ta-Si and enlarged centroid-Ta-Ta angles) is not observed in the full system. Whereas these angles differ by as much as 19° compared with the X-ray structure with the model system, they differ by no more than 4° with the full system. These results demonstrate that the BLYP plane wave computational scheme that was utilized is capable of reproducing the experimental geometries accurately. Moreover, the geometric distortions observed with the model complexes are due to the truncation of the ligands and not to the computational scheme adopted.

Although complex **2l** is calculated to be energetically most stable, it lies less than 1 kcal/mol lower than

Table 4. Best Fit rms Deviation between the X-ray Crystal Structure and the Calculated Structures

isomer	best fit rms deviation (Å) ^a
2a	0.08
2f	0.16
2j	0.17
2l	0.09

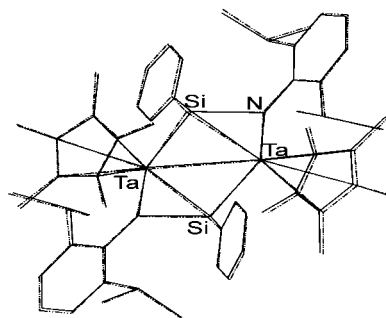
^a Best mass weighted fit rms deviation between the position of the heavy atoms in the X-ray structure and the calculated structures in Cartesian coordinates. The positions of the hydrogens were not included in the fitting procedure. Equally weighted values agree within 0.01 Å to the mass weighted values displayed here.

structure **2a**. This energy difference is within the error limits of the methodology employed. (Arguably the energy difference of 4 kcal/mol between **2f** and **2l** is also within this range.) Another density functional such as B3LYP^{20–22} or BP86^{23–25} may yield slightly different orderings of the isomers examined. Rather than reexamine the structures with different theoretical methodologies, we turn our attention to reconciling the present results with the experimental data.

Comparison with Experimental Data. In this section we compare the four candidate structures **2a**, **2f**, **2j**, and **2l** with the spectroscopic data. Of the four isomers that we have examined with the authentic ligand framework, only two possess hydrides in distinct environments, namely, **2j** and **2l**. Isomer **2j** contains two terminal hydrides bound to the same Ta center, whereas isomer **2l** contains one bridging and one terminal hydride. Even without considering the calculated relative energies of the two isomers (which reveal that isomer **2l** is most energetically favorable), isomer **2l** is the most promising candidate for two reasons. First, in complex **2j**, the two hydrides are both terminally bound to the same Ta center and might be expected to exchange on the NMR time scale. Second in **2j**, both hydrides are terminal in nature, whereas **2l** possesses hydrides in two distinct bonding schemes, one terminal and one bridging. This mixed terminal and bridging bonding scheme is more consistent with the two rather distinct ¹H NMR shifts observed at 11.63 and –0.99 ppm.

The calculated geometries of the four candidate isomers have been quantitatively compared with the experimental X-ray structure. The mass-weighted best fit rms deviation between Cartesian positions of the heavy atoms in the X-ray structure and each of the calculated structures is presented in Table 4. The symmetric isomer **2a** provides the best-fit geometry with an rms deviation of 0.08 Å. The asymmetric bridging/terminal structure **2l** provides a fit that is almost as good with an rms deviation of 0.09 Å. We note that the candidate isomers in which both hydrogens are bound exo to the cyclopentadienyl rings, **2f** and **2j**, have structural rms deviations roughly twice that of **2a** and **2l**.

Since **2l** is our best candidate, both in terms of relative energy and its agreement with the NMR data, we will compare its structure with the experimental structure in more detail. The agreement is striking, as illustrated

**Figure 7.** Best fit superposition of the X-ray structure and the calculated gas-phase structure of isomer **2l**. Hydrogens are not shown and were not included in the fit.**Table 5. Comparison of Experimental NOE Signal Intensities to Bond Distances in the Calculated Structure of 2l**

atom pair ^a	intensity ^b	calculated H–H distance (Å)
TaH (bridging, $\delta = -0.99$ ppm) to:		
TaH(terminal)	1	3.22
Si ¹ –H	1	3.18
both Cp* methyl protons	3/3	minimum = 2.60/3.02
ⁱ Pr ² –H _{down}	2	3.18
TaH (terminal, $\delta = -11.63$ ppm) to:		
TaH(bridging)	1	3.22
Si ¹ –H	4	2.69
Cp* ¹ methyl–H	3	2.72
<i>o</i> -Ph ¹ –H	3	2.68
ⁱ Pr ¹ –H _{up}	5	2.41
ⁱ Pr ¹ –H _{up,out}	2	3.88

^a Refer to Figure 4b. ^b The signal intensity was assigned a value of 1 through 5, where 1 represents a weak signal corresponding to an interatomic distance of around 3 Å or slightly above and 5 represents a strong signal corresponding to an interatomic distance of 2–2.4 Å.

in Figure 7, which depicts the best fit superposition of the X-ray structure and the calculated structure **2l**. The Ta–Ta bonding distance, which has been determined to be 2.85 Å from the X-ray analysis, is calculated to be 2.88 Å for **2l**. This is in better agreement than the calculated 2.78 Å Ta–Ta bond distance for the symmetric isomer **2a**. As previously stated, the X-ray structure revealed a symmetrical Ta₂N₂Si₂ ring with approximate C₂-symmetry. However, due to the asymmetric binding of the two hydrides in **2l**, the symmetry of this ring is necessarily broken. Although the ring asymmetry is not severe, the two Ta–Si bonds differ by 0.08 Å and the two Si–N bonds differ by 0.1 Å.

It is of interest to compare the NOE data of Figure 4 with results from the theoretical calculations. Table 5 compares the intensity of the NOE signals to the calculated H–H distances in the best candidate (**2l**). In this table we have assigned the low-field hydride ($\delta = 11.63$ ppm) to the terminal position and the high-field hydride ($\delta = -0.99$ ppm) to be bridging. Further, the signal intensities have been assigned values of 1 through 5, where 1 represents a weak signal corresponding to an interatomic distance of around 3 Å or slightly above and 5 represents a strong signal intensity corresponding to an interatomic distance of <2.4 Å. Table 5 reveals that the calculated H–H distances indeed fit the experimental NOE data very well. The only exception is that the coupling of protons on ⁱPr¹–Me_{up,out} (Figure

(20) Becke, A. D. *Chem. Phys.* **1996**, *104*, 1040.(21) Becke, A. D. *Chem. Phys.* **1993**, *98*, 5648.(22) Lee, C.; Yang, W.; Parr, R. G. *Phys. Rev. B* **1988**, *37*, 785.(23) Becke, A. *Phys. Rev. A* **1988**, *38*, 3098.(24) Perdew, J. P. *Phys. Rev. B* **1986**, *33*, 8822–8824.(25) Perdew, J. P. *Phys. Rev. B* **1986**, *34*, 7406.

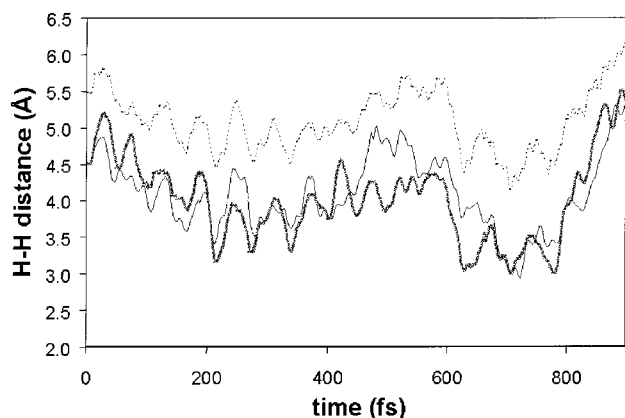


Figure 8. H–H distances of terminal hydride with $^1\text{Pr-Me}$ protons during a 400 K ab initio molecular dynamics simulation of **2l**.

4b) with the terminal hydride of the calculated structure yields a distance of 3.88 Å. Such an interatomic distance is too large to provide the signal observed. Possible explanations for the discrepancy include solvation effects (for which these calculations do not account) and finite temperature effects. To investigate the latter possibility, we performed a short (~ 1 ps) ab initio molecular dynamics simulation of the full complex (**2l**) at 400 K. Displayed in Figure 8 is the interatomic distance between the terminal hydride to each of the three protons of the $^1\text{Pr}^1\text{-Me}_{\text{up,out}}$ group. Figure 8 shows that during the course of the dynamics simulation, the H–H distance does fall within the 3 Å regime necessary to give rise to the observed NOE signal. This suggests that finite temperature effects may account for the weak NOE signal assigned to the terminal hydride– $^1\text{Pr}^1\text{-Me}_{\text{up,out}}$ group interaction.

Of the lowest energy candidate isomers, **2a**, **2f**, **2j**, and **2l**, only isomers **2l** and **2j** have nonequivalent hydrides. However, the calculated structure for candidate **2j** violates the NOE assignments in several key H–H distances. First and foremost, the two hydrides in structure **2j** are calculated to be only 1.8 Å apart, which is not in agreement with the weak NOE signal for this pair. Additionally, as previously stated, the high-field hydride appears to be in the area between the two Cp* ligands. In candidate **2j**, neither hydride is located between the Cp* ligands.

To summarize, the present calculations suggest that isomer **2l**, in which there is a terminal and bridging hydride, is the best candidate in terms of its relative energy and agreement with the available spectroscopic data. It is also the only isomer considered that is consistent with the NOE data, and its calculated geometry is in excellent agreement with the X-ray structure.

Theoretical Analysis of the Ta–Ta and Ta–Si Bonding. In this section the bonding within the Ta₂NSi ring is examined. In particular we describe the Ta–Ta bonding and the Ta–Si bonding from the standpoint of molecular orbital theory based on the calculated Kohn–Sham DFT wave functions. A qualitative measure of the strength of the covalent bond between two atoms can be provided by the Mayer bond order.¹⁸ These are displayed in Table 6 for isomers **a** and **l** for both the model and actual systems. We

Table 6. Selected Mayer Bond Orders²⁵ of the Calculated Isomers^a

bond ^b	model system		full system	
	3a	3l	2a	2l
Ta ² –Ta ¹	0.44	0.39	0.41	0.38
Ta ² –Si ²	0.33	0.35	0.41	0.43
Ta ² –Si ¹	0.30	0.24	0.24	0.20
Ta ¹ –Si ¹	0.33	0.37	0.41	0.42
Ta ¹ –Si ²	0.30	0.37	0.24	0.30
Ta ² –N ²	0.80	0.81	0.84	0.84
Ta ¹ –N ¹	0.80	0.87	0.84	0.88

^a Bond orders calculated from Kohn–Sham wave functions in the plane wave basis that are projected on an atom-centered basis.

^b Labeling scheme is defined in Figure 4b.

will examine the bonding in the symmetric isomer **a** and the asymmetric isomer **l**. Although we have concluded that the asymmetric isomer **l** is the best candidate, the two isomers are close in energy and the symmetry of isomer **a** simplifies the bonding analysis. Furthermore, variations in the bonding that arise from changes in ligand substitutions and hydride ligand positions are of interest.

Our analysis suggests that the bond between the Ta centers can be characterized as a weak σ -type bond. The calculated Ta–Ta bond orders for the complexes **2a**, **2l**, **3a**, and **3l** are all approximately 0.4. This compares to calculated values of approximately 0.8 for the Ta–N bonds, 0.3–0.4 for the Ta–Si bonds, 0.7 for the Si–N bonds, and 1.0 for the N–C(aryl) bonds. On the basis of this qualitative measure, we conclude that there is a weak Ta–Ta covalent bond. What can be characterized as the Ta–Ta bonding orbital is the HOMO for each of these complexes (see Supporting Information).

We now turn our attention to the Ta–Si bonding. Each silicon atom is bonded to both tantalum atoms, with nearly equivalent Ta–Si bond distances (2.61–2.79 Å). There are actually two types of Ta–Si bonds: one that can be considered as part of the Ta₂NSi ring system and one that “crosses” the ring. The “ring-crossing” Ta–Si bonds are depicted as the dashed bonds in Figure 4b. With the labeling scheme of Figure 4b, the ring-crossing bonds involve the Ta¹,Si² and Ta²,Si¹ atom pairs.

The calculated Mayer bond orders given in Table 6 show that there exists a weak ring-crossing Ta–Si bond. For the symmetric model complex **3a**, the calculated ring and ring-crossing Ta–Si bond orders are nearly equivalent at 0.33 and 0.30, respectively. This is also true for the asymmetric model complex **3l**, albeit with somewhat more variance. For the “full” complexes with Cp* and (2,6-¹Pr₂C₆H₃)NSiHPh ligands there is more discrepancy between the Ta²–Si² and Ta²–Si¹ bond orders, with the ring-crossing Ta–Si bond being much weaker. For example, in complex **2a** the Ta²–Si² and Ta²–Si¹ bond orders are 0.41 and 0.24, respectively. Interestingly, the Ta–Si ring-crossing bond distance is longer in the model complex than in the actual complex, which is opposite of what might be expected based on the calculated bond orders. This suggests that the short ring-crossing Ta–Si distance results from geometrical constraints of the ring system.

Conclusions

As expected, the Ta–H and Ta–Si bonds in Cp*(Ar–N=)Ta[Si(SiMe₃)₃]H are active toward σ -bond metath-

esis, as evidenced by the reaction with phenylsilane. Currently, however, the mechanism by which these bonds are cleaved in this reaction is unknown. Given the complexity of this reaction, we intend to address this issue in related tantalum compounds possessing only one active σ -bond (e.g., $\text{Cp}^*(\text{ArN}=\text{Ta}(\text{R})\text{Cl})$; $\text{R} = \text{H}$, $\text{Si}(\text{SiMe}_3)_3$).⁹

Of perhaps greater interest is the observed coupling of a silane with an imido ligand, to produce a Si–N bond. This coupling, and the accompanying cleavage of two Si–H bonds, ultimately results in the formation of a silanimine as a bridging ligand. The structural and theoretical data indicate that this ligand possesses very little (if any) Si–N double bond character and is therefore best viewed as a bifunctional silyl–amido ligand. Various mechanisms can be envisioned for this multistep process. One possible scheme involves σ -bond metathesis and/or oxidative addition–reductive elimination to introduce a –SiH₂Ph ligand. This silyl ligand could migrate to the imido nitrogen atom, to produce an amido ligand of the type –N(Ar)SiH₂Ph. To our knowledge, this type of migration has not been observed, but it seems quite conceivable, especially given observation of a corresponding hydrogen migration.¹¹ A Ta–N(Ar)SiH₂Ph complex could then undergo an intermolecular Si–H activation to produce the bridging silanimine ligand. Alternative schemes are based on the direct attack of silane on the Ta=NAr linkage, resulting in addition of the Si–H bond across the Ta=N double bond to give an (H)Ta–N(Ar)SiH₂Ph intermediate. This addition could proceed in a stepwise manner, as we have recently observed in the reaction of PhSiH₃ with a bent tantalum imido complex,²⁶ or in a concerted way, as has been proposed for the activation of hydrocarbons by group 4 imido complexes.²⁷

As suggested by the spectroscopic data and confirmed by the DFT calculations, the ditantalum dihydride complex **2** appears to be a rare example of a dinuclear metal complex possessing an asymmetrical distribution of hydride ligands, in a complex that would otherwise possess chemically equivalent metal centers (we are aware of no other examples).

The results from the DFT calculations on the entire 140-atom diamagnetic complex and the 127-atom paramagnetic complex are a convincing demonstration of the power of current state-of-the-art computational methods in the structure elucidation of novel transition metal complexes. Of particular note is the observation that the truncated ligand system (**3**) was inadequate to probe certain key aspects of the bonding in this system. This is particularly interesting given that simplified “surrogate” ligands are often used in theoretical investigations of inorganic and organometallic complexes.

Experimental Section

General Comments. All experiments were performed under dry nitrogen using standard Schlenk or drybox techniques. Solvents were distilled under nitrogen from sodium

benzophenone ketyl. Benzene-*d*₆ and toluene-*d*₈ were distilled from Na/K alloy. PhSiH₃ was dried over molecular sieves (4 Å) and distilled before use. The compound $\text{Cp}^*(\text{ArN}=\text{Ta})\text{[Si}(\text{SiMe}_3)_3\text{]H}$ was prepared according to a known procedure.^{8,9} Elemental analyses were performed by the Microanalytical Laboratory in the College of Chemistry at the University of California, Berkeley. Mass spectra (EI⁺) were recorded on a Micromass VG ProSpec instrument (ionization energy: 70 eV). FT-infrared spectra were recorded as KBr pellets (solids) on a Mattson FTIR 3000 instrument. ¹H, ²H, ¹³C, and ²⁹Si NMR spectra were recorded on Bruker AMX-300, AMX-400, or DRX-500 instruments, and chemical shifts are reported in ppm downfield from internal SiMe₄. For ¹H NOESY spectra, a mixing time of 0.8 s was applied. 2D ¹H,¹³C HMQC spectra were recorded as 2048 × 256 files using the BIRD sequence [$\pi/2(^1\text{H}) = 14.0 \mu\text{s}$; $\pi/2(^{13}\text{C}) = 6.4 \mu\text{s}$].²⁸ 1D ²⁹Si NMR spectra were obtained using a refocused INEPT pulse sequence with or without ¹H decoupling; delays were optimized for $J_{\text{SiH}} = 6.4 \text{ Hz}$ [$\pi/2(^1\text{H}) = 14.0 \mu\text{s}$; $\pi/2(^{29}\text{Si}) = 6.6 \mu\text{s}$]. 2D ¹H, ²⁹Si HMQ(B)C spectra were acquired as 2048 × 128 files with 16 transients accumulated per t_1 increment and were optimized for an assumed 4 Hz (125 ms) long-range J_{SiH} . Bruker XWINNMR software (ver. 2.1) was used for all processing.

X-ray Crystallography. Single-crystal analyses of **1** and **2** were carried out by Dr. Fred J. Hollander and Dr. Dana L. Caulder at the UC Berkeley CHEXRAY crystallographic facility. Measurements were made on a Bruker SMART CCD area detector with graphite-monochromated Mo K α radiation ($\lambda = 0.71069 \text{ \AA}$). Data were integrated by the program SAINT, corrected for Lorentz and polarization effects, and analyzed for agreement and possible absorption using XPREP. Empirical absorption corrections were made using SADABS. Structures were solved by direct methods and expanded using Fourier techniques. All calculations were performed using the teXsan crystallographic software package.

Reaction of $\text{Cp}^*(\text{ArN}=\text{Ta})\text{[Si}(\text{SiMe}_3)_3\text{]H}$ with Phenylsilane. To a freshly prepared solution of $\text{Cp}^*(\text{ArN}=\text{Ta})\text{[Si}(\text{SiMe}_3)_3\text{]H}$ (from $[\text{Cp}^*(\text{ArN}=\text{Ta})\text{Cl}(\mu\text{-H})_2]$ (400 mg, 0.38 mmol) and (THF)₃LiSi(SiMe₃)₃ (360 mg, 0.76 mmol) in hexanes (30 mL) was added PhSiH₃ (83 mg, 0.76 mmol). An instant color change from deep red to yellow was observed. The mixture was stirred at room temperature for 12 h while the color of the reaction solution gradually darkened to deep green. The solution was filtered, concentrated to half its original volume, and cooled to –30 °C. Three pure products were isolated from the reaction mixture by fractional crystallization: $[\text{Cp}^*(\text{ArN}=\text{Ta})\text{H}(\mu\text{-H})_2]$ as a yellow microcrystalline precipitate (15 mg, 4% based on Ta), paramagnetic **1** as yellow crystals (75 mg, 18% based on Ta), and diamagnetic **2** as dark green crystals in two crops (322 mg, 71% based on Ta).

Data for **1.** ¹H NMR (500 MHz, benzene-*d*₆, 73 °C): δ 10.5 (br s, 1 Ta–H), 7.65 (d, 2 H, *o*-Ph–H, $J = 6.5$), 7.16–6.82 (m, 9 Ar–H), 4.93 (s, 1 H, Si–H, $J_{\text{SiH}} = 220 \text{ Hz}$), 3.98, 3.60 (2 × br s, 2 ⁱPr–H), 3.41 (br s, 2 ⁱPr–H), 2.14, 1.95 (2 × s, 2 × 15 H, C₅Me₅), 1.48, 1.38, 1.24, 1.14 (4 × d, 4 × 3 H, ⁱPr–Me, $J = 6.8$), 1.3–0.8 (br s, 12 H, ⁱPr–Me), 0.2 (br s, 1 Ta–H). ¹³C NMR (101 MHz, benzene-*d*₆, shift values from ¹H,¹³C HMQC spectrum): δ 137.0 (*o*-Ph H), 124.0, 123.7, 122.3, 121.6 (Ar H), 27.5–23.0 (ⁱPr), 12.6 (C₅Me₅). ²⁹Si NMR (99 MHz, benzene-*d*₆, shift value from ¹H,²⁹Si HMQC spectrum): δ 9.7 (br). IR (KBr, cm^{–1}): 3051 w, 2958 s, 2910 m, 2866 m, 2173 br w, 1763 br m, 1653 br m, 1587 w, 1458 m, 1425 s, 1379 m, 1340 s, 1317 m, 1290 m, 1246 m, 1200 m, 1109 m, 1028 w, 966 w, 933 m, 829 sh, 773 m, 798 m, 754 m, 739 m, 722 w, 702 m, 474 w. MS: m/z 1090 (95, [M]⁺), 1086 (100), 1041 (19), 980 (28), 935 (10), 591 (13), 552 (15), 541 (16), 489 (23), 466 (12), 444 (12). $\mu_{\text{eff}} = 2.0$ (Evans' method).¹⁷ Anal. Calcd for C₅₀H₇₂N₂SiTa₂ (1091.12): C, 55.04; H, 6.65; N, 2.57. Found: C, 54.75; H, 6.42; N, 2.51.

Structural Determination of **1.** Suitable crystals were grown from pentane solution at –30 °C. A fragment (0.25 ×

(26) Gountchev, T. I.; Tilley, T. D. *J. Am. Chem. Soc.* **1997**, *119*, 12831.

(27) (a) Cummins, C. C.; Baxter, S. M.; Wolczanski, P. T. *J. Am. Chem. Soc.* **1988**, *110*, 8731. (b) Cummins, C. C.; Schaller, C. P.; Van Duyn, G. D.; Wolczanski, P. T.; Chan, A. W. E.; Hoffmann, R. *J. Am. Chem. Soc.* **1991**, *113*, 2985. (c) Walsh, P. J.; Hollander, F. J.; Bergman, R. G. *J. Am. Chem. Soc.* **1988**, *110*, 8729. (d) Cundari, T. R. *J. Am. Chem. Soc.* **1992**, *114*, 10557.

0.23 × 0.15 mm) was cut from a yellow platelike crystal, mounted on a quartz fiber using Paratone N hydrocarbon oil, and cooled under a nitrogen stream in the diffractometer. Non-hydrogen atoms were refined anisotropically. The silicon hydrogen (H70) and the hydrides (H71, H72) were located in the difference Fourier map and refined with fixed thermal parameters. All other hydrogen atoms were included in calculated idealized positions but not refined. The final refinement cycle converged at $R = 0.025$ and $R_w = 0.028$.

Data for 2. ^1H NMR (500 MHz, benzene- d_6 , 25 °C): δ 11.63 (dd, 1 H, $\text{Ta}^1\text{-H}_{\text{terminal}}$, $J = 5.5, 2.3$), 7.63 (m, 2 H, $o\text{-Ph}^1\text{H}$), 7.55 (m, 2 H, $o\text{-Ph}^2\text{-H}$), 7.22 (dd, 1 H, $m\text{-Ar}^1\text{-H}_{\text{down}}$, $J = 7.6, 1.8$), 7.19 (dd, 1 H, $m\text{-Ar}^2\text{-H}_{\text{down}}$, $J = 7.6, 1.8$), 7.12 (m, 1 H, $p\text{-Ar}^1\text{-H}$), 7.10 (m, 2 H, $m\text{-Ph}^2\text{-H}$), 7.09 (m, 1 H, $p\text{-Ph}^2\text{-H}$), 7.08 (m, 1 H, $m\text{-Ar}^1\text{-H}_{\text{up}}$), 7.05 (m, 1 H, $p\text{-Ar}^2\text{-H}$), 7.00 (m, 1 H, $p\text{-Ph}^1\text{-H}$), 6.99 (m, 1 H, $m\text{-Ar}^2\text{-H}_{\text{up}}$), 6.98 (m, 2 H, $m\text{-Ph}^1\text{-H}$), 5.23 (dd, 1 H, $\text{Si}^1\text{-H}$, $J = 5.5, 2.9$, $^1J_{\text{Si,H}} = 215$), 5.09 (s, 1 H, $\text{Si}^2\text{-H}$, $^1J_{\text{Si,H}} = 193$), 3.59 (sept., 1 H, $^i\text{Pr}^2\text{-H}_{\text{down}}$, $J = 6.7$), 3.10 (sept., 1 H, $^i\text{Pr}^2\text{-H}_{\text{up}}$, $J = 6.7$), 3.06 (sept., 1 H, $^i\text{Pr}^1\text{-H}_{\text{up}}$, $J = 6.7$), 3.03 (sept., 1 H, $^i\text{Pr}^1\text{-H}_{\text{down}}$, $J = 6.7$), 2.01 (s, 15 H, Cp^{*2}), 1.91 (s, 15 H, Cp^{*1}), 1.68 (d, 3 H, $^i\text{Pr}^2\text{-Me}_{\text{down,out}}$, $J = 6.7$), 1.67 (d, 3 H, $^i\text{Pr}^2\text{-Me}_{\text{down,in}}$, $J = 6.7$), 1.53 (d, 3 H, $^i\text{Pr}^1\text{-Me}_{\text{down,in}}$, $J = 6.7$), 1.44 (d, 3 H, $^i\text{Pr}^1\text{-Me}_{\text{down,out}}$, $J = 6.7$), 1.13 (d, 3 H, $^i\text{Pr}^2\text{-Me}_{\text{up,out}}$, $J = 6.7$), 0.90 (d, 3 H, $^i\text{Pr}^1\text{-Me}_{\text{up,out}}$, $J = 6.7$), 0.56 (d, 3 H, $^i\text{Pr}^1\text{-Me}_{\text{up,in}}$, $J = 6.7$), 0.24 (d, 3 H, $^i\text{Pr}^2\text{-Me}_{\text{up,in}}$, $J = 6.7$), -0.99 (pseudo-t, 1 H, Ta-H-Ta , $J = 2.7$). $^{13}\text{C}\{^1\text{H}\}$ NMR (126 MHz, benzene- d_6): δ 151.11, 150.44, 144.33, 141.74, 141.66, 140.84, 139.09, 138.53 (Ar/Ph C), 139.29 ($o\text{-Ph}^2$ CH), 137.75 ($o\text{-Ph}^1$ CH), 129.12 ($m\text{-Ar}^1$ CH_{up} , and $m\text{-Ar}^2$ CH_{up}), 127.94 ($m\text{-Ph}^1$ CH), 127.66 ($m\text{-Ph}^2$ CH), 124.47 ($p\text{-Ph}^2$ CH), 124.28 ($m\text{-Ar}^2$ CH_{down} , and $p\text{-Ar}^1$ CH), 124.22 ($m\text{-Ar}^1$ CH_{down}), 124.10 ($p\text{-Ph}^1$ CH), 123.76 ($p\text{-Ar}^2$ CH), 113.69, 110.52 (C_5Me_5), 29.17 ($^i\text{Pr}^2$ $\text{Me}_{\text{down,in}}$), 28.87 ($^i\text{Pr}^1$ $\text{Me}_{\text{down,in}}$), 28.65 ($^i\text{Pr}^1$ CH_{down}), 28.02 ($^i\text{Pr}^2$ CH_{down}), 27.82 ($^i\text{Pr}^2$ CH_{up}), 27.52 ($^i\text{Pr}^1$ CH_{up}), 27.02 ($^i\text{Pr}^2$ $\text{Me}_{\text{up,in}}$), 25.94 and 25.92 ($^i\text{Pr}^1$ $\text{Me}_{\text{up,out}}$, and $^i\text{Pr}^1$ $\text{Me}_{\text{down,out}}$), 25.57 and 25.54 ($^i\text{Pr}^2$ $\text{Me}_{\text{up,out}}$, and $^i\text{Pr}^2$ $\text{Me}_{\text{down,out}}$), 25.17 ($^i\text{Pr}^1$ $\text{Me}_{\text{up,in}}$), 13.96 (C_5Me_5^2), 12.92 (C_5Me_5^1). $^{29}\text{Si}\{^1\text{H}\}$ NMR (99 MHz, benzene- d_6): δ 14.2, -7.6. IR (KBr, cm^{-1}): 3049 m, 2959 s, 2904 s, 2869 s, 2724 w, 2181 m, 2145 sh, 1950 vw, 1906 vw, 1792 w, 1648 vw, 1622 vw, 1588 w, 1535 vw, 1459 m, 1425 s, 1380 m, 1360 w, 1314 m, 1238 m, 1191 m, 1105 m, 1027 m, 918 m, 858 sh, 839 m, 806 m, 786 m, 756 m, 733 m, 700 m, 606 w, 549 w, 526 m, 474 w, 432 m. MS: m/z 1196 (100, $[\text{M}]^+$). UV-vis (THF): λ_{max} 392 nm. Anal. Calcd for $\text{C}_{56}\text{H}_{78}\text{N}_2\text{Si}_2\text{Ta}_2$ (1197.32): C, 56.18; H, 6.57; N, 2.34. Found: C, 55.95; H, 6.31; N, 2.44.

Structural Determination of $2 \cdot \frac{2}{3}\text{C}_6\text{H}_{14}$. Suitable crystals were grown from hexane solution at -30 °C. A fragment (0.41 × 0.30 × 0.05 mm) was cut from a green blade-shaped crystal, mounted on a quartz fiber using Paratone N hydrocarbon oil, and cooled under a nitrogen stream in the diffractometer. Two regions of highly disordered solvent molecules (hexane) were modeled as three half-occupancy carbons and as 10 quarter-occupancy carbons, respectively, giving a total of 2/3 of a hexane molecule. Non-hydrogen atoms were refined anisotropically, except for those that were part of the disordered solvent region, which were refined isotropically. Hydrogen atoms were included in calculated idealized positions but not refined. The final refinement cycle converged at $R = 0.036$ and $R_w = 0.046$.

Computational Details. Kohn-Sham density functional theory²⁹ calculations as embodied in the Car-Parrinello ab initio molecular dynamics method³⁰ and pseudopotential theory³¹ have been performed with the program CPMD.³² The BLYP density functional was utilized as developed by Becke²³ for the exchange component and by Lee, Yang, and Parr²² for the correlation component.

The valence orbitals are expanded in a basis of plane waves with a kinetic energy cutoff of 70 Ry. A face-centered cubic (fcc) super cell of edge 18 and 22 Å was utilized for the model diamagnetic complex, **3**, and the full diamagnetic complex, **2**, respectively. An fcc cell of length 23 Å was used for the calculations of the paramagnetic complex, **1**. For C, N, and Si only the valence electrons are treated explicitly. The nonlocal, norm-conserving pseudopotentials of Martins and Trouiller³³ have been applied to represent the effects of the ionic cores. The following radial cutoffs were used: $r_s = r_p = 1.23$ au for carbon, $r_s = r_p = 1.12$ au for nitrogen, and $r_s = 1.9$; $r_p = r_d = 2.1$ au for silicon. For tantalum we constructed a semi-core pseudopotential such that the 5s, 5p, 5d, and 6s electrons were treated explicitly. Using this pseudopotential with a kinetic energy cutoff of 70 Ry, the calculated bond distance of 1.677 Å in TaO compares well with the experimental gas-phase electron diffraction value of 1.6875 Å.³⁴ We have examined the convergence properties of the Ta pseudopotential by repeating the TaO calculations at 60, 80, 90, and 120 Ry. Both the total energy and Ta-O bond distance show smooth and steady convergence. At 70 Ry, the TaO bond distance is only 0.004 Å larger than the distance obtained with a high energy cutoff of 120 Ry. A spin-restricted formalism was utilized for all calculations of the diamagnetic complexes, whereas the spin-unrestricted formalism has been utilized for all calculations of the paramagnetic species, **1**. Ab initio molecular dynamics simulations were performed with a time step of 5 au and fictitious mass for the electronic degrees of freedom of $\mu = 500$ au. To calculate the Mayer bond orders,¹⁸ the one-electron Kohn-Sham orbitals in the plane wave basis were projected onto a minimal, atom-centered basis consisting of the atomic pseudo wave functions.

All calculations were performed on the IBM-SP (160 MHz nodes) of the Competence Center for Computational Chemistry, C⁴, at the ETH in Zürich. For calculations on the diamagnetic model system **3**, which consists of 34 atoms and 102 electrons, each molecular dynamics time step required about 22 s on 16 nodes. For the full diamagnetic complex **2**, which contains 140 atoms and 346 electrons, each time step required about 77 s on the same number of nodes.

Acknowledgment. We thank the National Science Foundation for their generous support of this work. Dr. Fred J. Hollander and Dr. Dana L. Caulder are gratefully acknowledged for the determination of the crystal structures, and Tomislav I. Gountchev is acknowledged for recording the high-temperature NMR spectra of compound **2**. U.B. is indebted to the Schweiz. Nationalfonds and the Novartis Stiftung for postdoctoral fellowships. T.K.W. would like to thank the Natural Sciences and Engineering Council of Canada for a postdoctoral fellowship. U.R. acknowledges an ETH research grant under No. TH 23/97-4 Fonds Nr. 0-28472-99.

Supporting Information Available: Tables of crystal, data collection and refinement parameters, atomic coordinates, bond distances, bond angles, and anisotropic displacement parameters for compounds **1** and $2 \cdot \frac{2}{3}\text{C}_6\text{H}_{14}$. A plot of the HOMO of isomer **21**. This material is available free of charge via the Internet at <http://pubs.acs.org>.

OM000455X

(28) Bax, A.; Subramanian, S. *J. Magn. Reson.* **1986**, *67*, 565.

(29) Kohn, W.; Sham, L. J. *Phys. Rev.* **1965**, *A140*, 1133.

(30) Car, R.; Parrinello, M. *Phys. Rev. Lett.* **1985**, *55*, 2471.

(31) Kleinman, L.; Bylander, D. M. *Phys. Rev. Lett.* **1982**, *48*, 1425.

(32) Hutter, J.; Ballone, P.; Bernasconi, M.; Focher, P.; Fois, E.; Goedecker, S.; Parrinello, M.; Tuckerman, M. *CPMD*; Max-Planck-Institut für Festkörperforschung, Stuttgart, Germany, and IBM Zürich Research Laboratory, 1998.

(33) Trouiller, N.; Martins, J. L. *Phys. Rev. B* **1991**, *43*, 1993.

(34) Lide, D. R. *CRC Handbook of Chemistry and Physics*, 76th ed.; CRC Press: Boca Raton, FL, 1996.